Experimental Study of an Impingement Cooling Jet Array Using an Infrared Thermography Technique

Andrew Schroder*

University of Cincinnati, Cincinnati, OH, 45221, U.S.A.

Shichuan Ou†

U.S. Air Force Research Laboratory, Wright Patterson Air Force Base, OH, 45433, U.S.A.

Urmila Ghia‡

University of Cincinnati, Cincinnati, OH, 45221, U.S.A.

An experimental test facility has been designed, constructed, and commissioned for studying the convective heat transfer of an array of 55 impingement jets with a constant heat flux boundary condition. Spatial variation in time averaged Nusselt number as well as spanwise time averaged Nusselt number are presented for jet Reynolds numbers of 4,000, 8,000, 12,000, and 15,000 for a jet to target standoff distance of z/D=3. For each of these configurations the exit flow has also been varied to include both a single exit and double exit configuration. The time and overall area averaged Nusselt number is presented as a function of jet Reynolds number. The results show that the time averaged Nusselt number increases with increasing jet Reynolds number in both the local and spanwise averaged values. The single exit configuration provides lower values of local and spanwise averaged Nusselt number for all jet Reynolds numbers studied compared to the double exit configuration. This reduction is caused by more cross flow accumulation while it moves toward the exit.

*Graduate Student, University of Cincinnati

†Aerospace Engineer, Propulsion Directorate, U.S. Air Force Research Laboratory

‡Professor of Mechanical Engineering, School of Dynamic Systems, University of Cincinnati

Nomenclature

Symbols

$\alpha_{film,natural}$	thermal diffusivity based upon film temperature, natural convection side, m^2/s
β	expansion coefficient, $(1/T_{s,spanwise}(x,t))$, $1/K$
μ	absolute viscosity, $N*s/m^2$
$\nu_{film,natural}$	kinematic viscosity based upon film temperature, natural convection side, m^2/s
π	ratio of the circumference of a circle to its diameter
$\dot{m}$	total mass flow rate through all impingement jet nozzles, kg/s
D	impingement jet nozzle diameter, m
g	combined gravitational and centrifugal acceleration on the earth's surface, m/s^2
H	height of the imageable region of the foil heater, H
$h(x,y,t)$	local impingement jet convective heat transfer coefficient, $W/(m^2*K)$
I	current, $Amps$
$k(x,y,t)$	local thermal conductivity based on the local film temperature, $W/(m*K)$
l	heated foil length, m
N	total number of impingement jet nozzles
$Nu(x,y,t)$	local Nusselt number based on the jet nozzle diameter, $\left(\frac{h(x,y,t)*D}{k(x,y,t)}\right)$
Nu_{mean}	time and area averaged Nusselt number
$Nu_{natural}(x,y,t)$	Nusselt number for natural convection
q''_{foil}	foil heater heat flux, W/m^2
$q''_{losses}(x,y,t)$	heat losses on the imaged side of the foil, W/m^2
$Ra_y(x,y,t)$	Rayleigh number, $\left(\frac{g*\beta*(T_{s,spanwise}(x,t)-T_{ambient})*y^3}{\alpha_{film,natural}*\nu_{film,natural}}\right)$
Re_{jet}	Reynolds number based on the jet nozzle diameter
t	time, s
$T_s(x,y,t)$	local foil surface temperature, K
$T_{ambient}$	static temperature of the ambient air in the test cell, K
$T_{film}(x,y,t)$	local film temperature, $\left(\frac{T_{upstream}+T_s(x,y,t)}{2}\right)$, K
$T_{s,spanwise}(x,t)$	spanwise average surface temperature, $\left(\frac{1}{H}\int_0^H T_s(x,y,t)dy\right)$, K
$T_{upstream}$	average fluid temperature measured in the pressure chamber, K
V	voltage drop across the foil heater, $Volts$
w	heated foil width, m
x	horizontal dimension, m
y	vertical dimension, m
z	normal dimension, m

I. Introduction

Gas turbine engine designs are increasingly pushing the structural and thermal limitations of today's materials. In a gas turbine engine, as in any heat engine, higher temperature and higher pressure cycles lead to higher efficiency and higher power density. Gas turbine engines typically use high thermal conductivity metals due to their cost, durability, strength and toughness. There is an increasing push for the use of Ceramic Matrix Composite (CMC) materials in gas turbine hot sections; however, CMCs also have temperature limitations. Regardless of the maximum service temperature of the material, heat transfer must be carefully controlled in order to keep parts from overheating.

Internal cooling of gas turbine hot section components, such as turbine blades, is commonly performed through the combination of impingement cooling and serpentine channels. This research is focused on impingement cooling. Impingement cooling has the advantage of a thin boundary layer due to the stagnation point flow when the jet core impacts the target surface. Additionally, mixing of the cool supply air and the hotter, spent air is reduced due to the separation of these two fluids by an impingement nozzle plate. Unfortunately, when large arrays of impingement jets are implemented inside a gas turbine blade, cross flow

effects from spent jet air reduce the cooling effectiveness of downstream jets. The jet is bent, the strength of the jet is reduced, and the spent air engages in additional mixing prior to impacting the surface to be cooled.

The earliest techniques utilized arrays of thermocouples to study the spatially dependent heat transfer coefficients on an impingement target surface.[1,2] The thermocouple technique can provide data at some discrete locations under consideration but does not allow for temperature measurement on the majority of the target surface. Later developments primarily utilized a transient liquid crystal thermography technique.[3--6] The transient liquid crystal technique provides very detailed local heat transfer data but does not allow for time averaging of the convective heat transfer coefficient, rather, it assumes that the convective heat transfer coefficient is independent of time. Additionally, the transient liquid crystal technique requires complex liquid crystal color vs temperature calibration procedures, sensitive test procedures and custom data reduction software. These transient techniques typically utilize recirculation loops in order to heat the supply air to an appropriate temperature.

In order to overcome these complexities and limitations, a new type of test rig has been developed for studying the convective heat transfer coefficient of impingement jets in the presence of cross flow. This new, compact test rig utilizes a steady state infrared thermography technique which allows for the determination of unsteady, as well as time averaged convective heat transfer coefficients with respect to position on the impingement surface.

The present work focuses on cylindrical impingement jet nozzles due to structural and manufacturing requirements of the gas turbine blade. Although the application of impingement cooling to gas turbine blades is of primary interest, the geometry studied was much simpler than typically found in a gas turbine blade. The impingement jet nozzles were arranged in a rectangular pattern. The target surface was flat. The impingement jet nozzle plate was primarily rectangular in cross section. In an application found in an actual turbine blade, curved nozzle plates and target surfaces would be required, and unequal placement of impingement jet nozzles may be necessary due to the cooling needs of the turbine blade. In addition, no rotational affects were studied in the present work. The purpose of the present study is to better characterize the effects of the cross flow and jet-to-jet interactions on jet performance in impingement jet arrays.

II. Test Rig, Test Sequence, and Post Processing Methodology

A facility was developed which utilized an electrically heated foil cooled by impinging jets. Due to the thin nature of the foil, an infrared camera was able to image the side of the foil opposite of impingement. A schematic of the layout of the test rig is also shown in Figure 1.

Figure 2 depicts a cross sectional schematic of the inlet diffusers and the test section. The test rig is supplied with room temperature air via a shop air supply system. The air supply enters the test section at the transition duct. The transition duct contains a series of diffusers through which the air passes, and then enters the pressure chamber. The transition duct is manufactured primarily of aluminum. When the air reaches the pressure chamber it is at a nearly uniform velocity and static pressure throughout due to the series of meshes which serve to condition the flow.

The walls of the remainder of the test section were manufactured from an optically transparent polycarbonate. The impingement jet nozzle plate was designed with 5 rows of 11 nozzles, laid out in a rectangular pattern. Figures 3(a) and 3(b) show dimensional top and side views at sectional planes placed at the center of the test section. Each impingement jet nozzle consisted of a simple cylindrical hole drilled into the nozzle plate. The holes were designed with sharp edges, however, a deburring process used during manufacturing did introduce a very small radius at the edges of the holes. The hole diameter (D) is 4.76mm. The non-dimensional spacing of the holes in the nozzle plate is such that centers of the holes are placed at a fixed regular spacing of x/D = 3 and y/D = 3. Hole spacing was motivated by the lack of results available in the public domain for such a configuration. Although the distance between the hole centers in the array was the same, the distance between the centerline of the outermost rows and the sidewalls was not. In order to maintain periodicity with the sidewalls, the distance between the sidewalls and the centerline of the outer rows should be one half the distance between the centerlines of all other holes in the interior of the array. Due to mounting constraints of the heated foil, the distance between the sidewalls and the centerline of the outermost rows had to be increased to y/D=4.08, rather than the ideal periodic spacing of y/D=1.5. The spacing between the sidewalls and the centerline of the outermost rows is illustrated in Figures 3(a) and 3(b). The non-dimensional standoff distance from the nozzle exit to the foil (target) was three nozzle diameters (z/D=3). The nozzle plate and the inlet supply are setup in a ‘‘co-flow” arrangement. After passing through the nozzle plate and impacting

the impingement surface, the spent jet air can exit in two directions. The exits are maintained at atmospheric pressure. One of the two exists could be blocked with a spacer forcing all air to exhaust in one direction. As a result, the cross flow was increased.

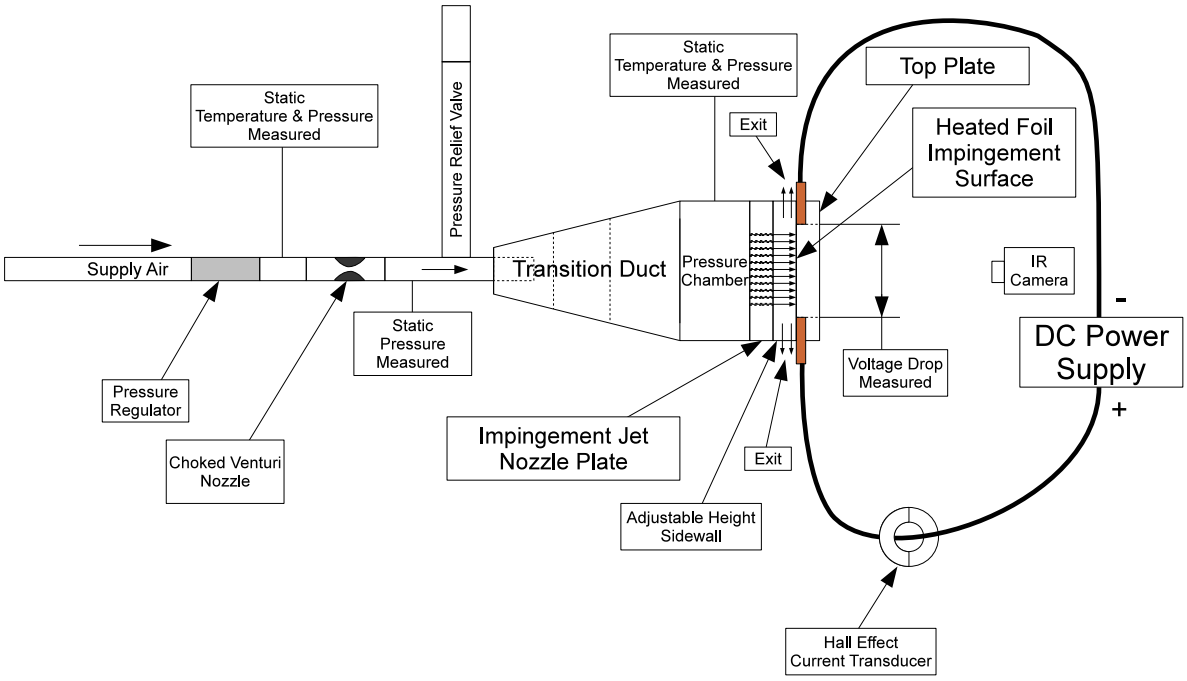

Figure 1. Schematic of the Test Rig

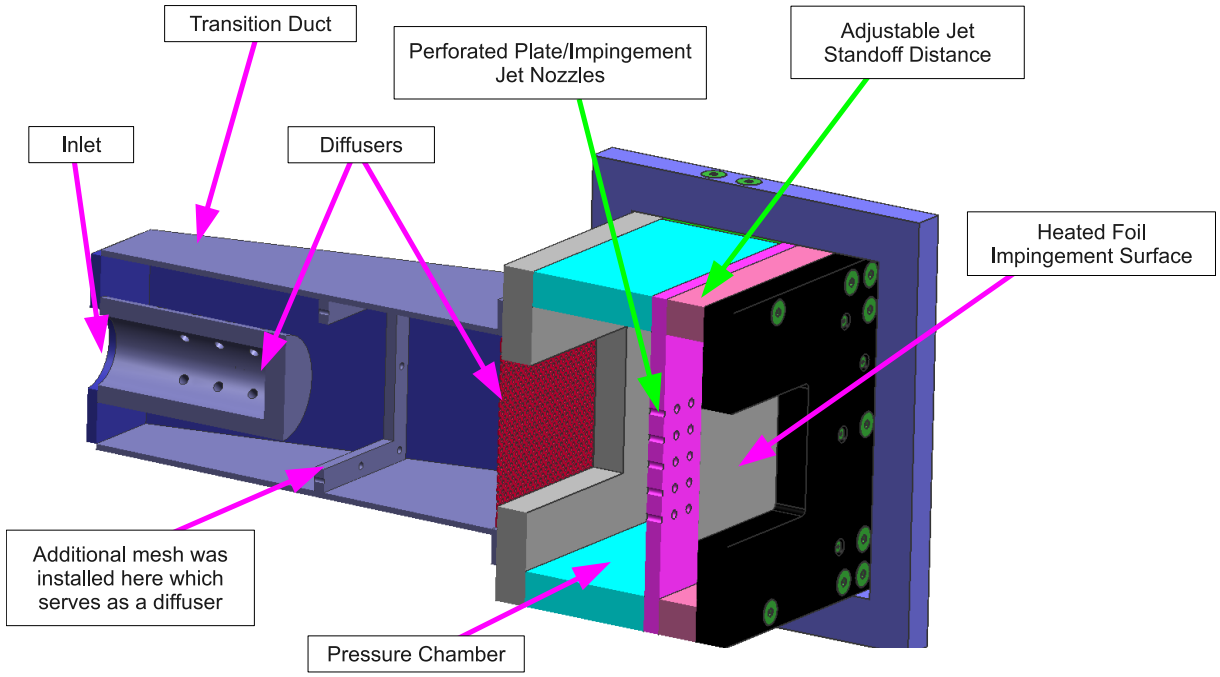

Figure 2. Rendering of a Cross Sectional View of the Test Section

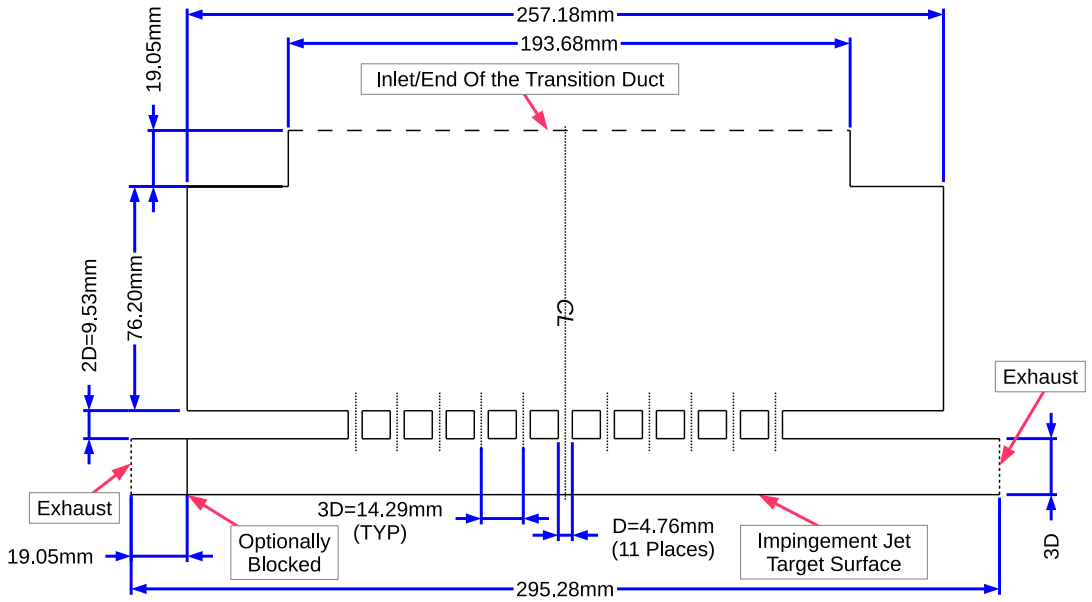

(a) Top

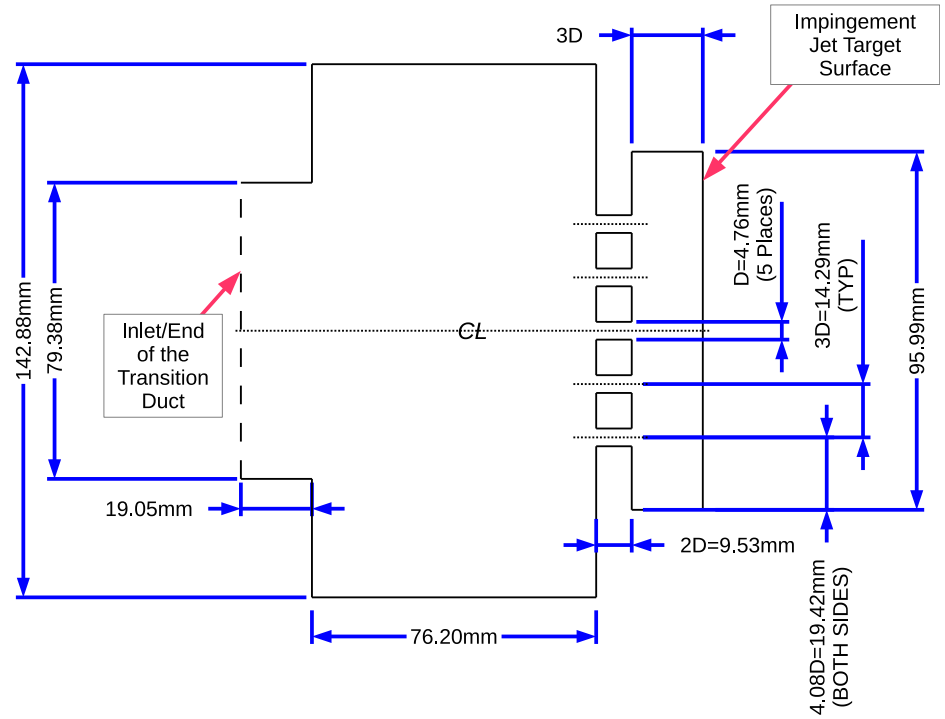

(b) Side

Figure 3. Sectional Views of the Test Section Flow Path

The heated foil consisted of a 38.1μm thin stainless steel foil placed on the inner side of the polycarbonate top plate. An opening was cut in the polycarbonate top plate so that the opposite side of the foil could be imaged. An intricate soldering process was developed to attach the thin stainless steel foil to the much thicker set of copper busbars (which connected to the DC electrical power supply). A tensioning process was used during assembly to ensure that the foil would not distort due to the stagnation pressure of the impingement jets or thermal expansion. The copper busbars were embedded into a grove which was machined into the polycarbonate top plate. With the careful integration of the busbars and tensioning of the foil, the target surface remained flat and smooth during testing.

Electrical current was supplied to the foil heater by a digitally controlled American Reliance PQ40-165

DC power supply. DC electrical current was measured via a CTL-201/200 Hall effect current transducer manufactured by Ohio Semitronics. Due to Joule heating, the foil was heated volumetrically by passing the DC electrical current through it. Foil width (w) was measured during the assembly process. No volumetric resistivity of the stainless steel foil was specified by the manufacturer. The volumetric resistivity of stainless steel foil is dependent upon the alloy of stainless steel, as well as the temperature. In addition, precise verification of uniform foil thickness was difficult, as the foil was very thin and flexible. Due to these uncertainties, the heat flux was formulated in terms of the voltage drop across the foil and the current passing through the foil, rather than the current passing through the foil and the resistance of the foil. The heated foil surface heat flux can be represented by

$$q''_{foil} = \frac{I * V}{l * w} \tag{1}$$

The voltage drop (V) across the foil heater was measured by soldering two 0.255mmø (30AWG) wires at each end of the measurement domain, and the distance (l) between the two attachment points was measured.

In order to establish the impingement jet nozzle Reynolds number (Re_{jet}), the nozzle mass flow rate was measured rather than measuring both the mean nozzle flow velocity and the mean nozzle fluid density. Rather than measuring the the individual Reynolds numbers for flow through each impingement jet nozzle, the total mass flow rate through all impingement jet nozzles was measured, and Re_{jet} was computed based upon the area weighted average impingement jet nozzle mass flow rate. In terms of mass flow rate, the impingement jet nozzle Reynolds number can be represented as

$$Re_{jet} = \frac{4\dot{m}}{N\mu\pi D} \tag{2}$$

where $\dot{m}$ is the total mass flow rate through all impingement jet nozzles, N is the total number of jets, μ is the fluid viscosity, and D is the impingement jet nozzle diameter. Mass flow rate was measured via a sonic converging diverging nozzle (choked venturi nozzle) with a throat diameter of 6.35mm. With air as the working fluid, the fluid viscosity was evaluated using the Sutherland Law for viscosity. Due to the low fluid Mach numbers inside of the impingement jet nozzles (less than 0.15 for all test cases), the temperature of the fluid inside the impingement jet nozzles was assumed to be at the same temperature as the fluid upstream in the pressure chamber, $T_{upstream}$. With a Mach number less than 0.15 for all test cases, the difference between the static temperature and the total temperature is estimated to be less than 0.45%.

Surface temperature measurement was performed via a FLIR ThermoCAM SC3000 infrared (IR) camera, which featured an image resolution of 320 by 240 pixels. The imaged surface was painted with a black paint. A similar procedure was used as was by Ou and Rivir[7] to measure the paint emissivity. The measured emissivity of approximately 0.96 was in agreement with previous experience. Because of the thin nature of the heated foil impingement surface, both sides of the foil were assumed to be at an equal temperature. With this assumption, the side of the foil opposite of impingement was imaged with the IR camera, obtaining a spatial temperature distribution ($T_s(x, y, t)$) on the foil. The IR camera was attached to a Windows XP workstation via a PCI frame grabber card, and the FLIR ThermaCAM Researcher software package was utilized to record each image. For each test case, 1500 frames were recorded at a frame rate of 43.78 frames/second and the temperature distribution for each frame was converted to the MATLAB data file format for post processing.

Although the IR camera records images with a size of 320 pixels x 240 pixels, the measurement domain was reduced because the aspect ratio of the measurement domain did not match the aspect ratio of the IR camera. The measurement domain was reduced additionally due to excessive thermal conduction near the connection of the thick copper busbar to the thin stainless steel foil. Because of this effect, the measurement domain had to be truncated such that an appropriate attenuation of this heat sink effect was achieved. Unfortunately, this reduced the field of view such that only 45 impingement jets could be imaged, rather that the total 55 present in the test rig. In the high cross flow test case (single exit), the total number of jets imaged was further reduced to 40 due to bending of the jets outside of the measurement domain due to high cross flow. The resultant image resolution was approximately 1.8 pixels/mm (0.56mm/pixel).

The fluid temperature was measured in the pressure chamber of the test rig using 0.127mmø (36AWG) type J thermocouples. Three thermocouples were utilized in the pressure chamber, and the measured values were averaged. Because this temperature is measured upstream of the impingement jet nozzles, this average temperature is designated $T_{upstream}$. For all cases there was less than 0.5 K variation between the maximum and minimum temperatures measured in the pressure chamber.

Except for the IR camera, all instrumentation was attached to a National Instruments SCXI series signal conditioning and PXI series analog to digital (A/D) conversion hardware. Data was set to be recorded at 200 samples/second for a period of 1 second. The data was then time averaged in order to eliminate any noise introduced by the instrumentation, wiring, etc. The National Instruments LabView software running on a Microsoft Windows XP workstation was used to record data, perform averaging, calculate Reynolds number and heat flux, and to monitor all parameters.

Due to the careful design of the test rig and the steady state infrared thermography technique, the test sequence proved to be very simple and straightforward. The test sequence began by powering on the supply air and slowly regulating the pressure until the desired Reynolds number is achieved. Once the desired Reynolds number was achieved, electrical power was supplied to the DC power supply and the unit was powered on. When the maximum temperature of the foil reached approximately 75°C and stabilized, the heat flux was held constant. Once the temperature had stabilized, data was then recorded by both the LabView system and the IR camera workstation. It took about 1 hour to finish a test case.

Once the test sequence was complete, the results were post processed numerically for each exit flow configuration and jet Reynolds number using the software application MATLAB. The convection coefficient on the target surface ($h(x,y,t)$) was evaluated using the expression

$$h(x,y,t) = \left(q''_{foil} - q''_{losses}(x,y,t)\right) \frac{1}{(T_s(x,y,t) - T_{upstream})} \tag{3}$$

Using Equation 3, the Nusselt number ($Nu(x,y,t)$), the non-dimensional heat transfer coefficient could then be evaluated. The term $q''_{losses}(x,y,t)$ included estimates for both radiation and natural convection losses on the imaged side of the foil. Each of these losses was estimated to account for 3-4% of the total heat generated by of the foil heater. When estimating the radiative losses, a local surface temperature ($T_s(x,y,t)$) was used with the Stefan-Boltzmann law. When estimating the natural convection heat losses, the natural convection coefficient was estimated using a correlation for Nusselt number for laminar free convection of an isothermal vertical surface represented by[8]

$$Nu_{natural}(x,y,t) = 0.387 Ra_y(x,y,t)^{1/4} \tag{4}$$

The foil heater surface is not isothermal, but was presumed to locally behave as an isothermal surface because the dominant factor driving the temperature on the foil heater was forced convection due to the impingement jets, rather than natural convection. Because the natural convection correlation assumed the vertical surface was isothermal, the evaluation of the Rayleigh number utilized a spanwise average surface temperature ($T_{s,spanwise}(x,t)$) for each specific x position. This spanwise averaging approach does not rigorously account for the convection coefficient's variation due to the variation in temperature in the vertical direction, however, it was used because the correlation utilized was for a surface with no variation in surface temperature in the vertical direction and because the dependence of Nusselt number on surface temperature is relatively weak (due to the 1/4 power). With lateral conduction in the foil assumed to be negligible, each horizontal position was assumed to act as an independent isothermal surface for the purpose of estimating the natural convection coefficient. Although a spanwise average surface temperature was used to evaluate the Rayleigh number, the Rayleigh number, by its definition, is still dependent upon the local vertical dimension (y). A film temperature based upon this spanwise average surface temperature ($T_{s,spanwise}(x,t)$) was used when evaluating fluid properties for the natural convection coefficient estimates. The natural convection losses were then estimated using Newton's law of cooling. The temperature difference based upon the local surface temperature ($T_s(x,y,t)$) was used due to the strong dependence of Newton's law of cooling on the surface temperature. For a more detailed discussion of the evaluation of $q''_{losses}(x,y,t)$, the source code of the MATLAB scripts, the design of the test rig, as well as the test sequence, please refer to the Master's thesis of Andrew Schroder.[9]

Estimates of the uncertainty in the measured target surface Nusselt number and jet Reynolds number were conducted using the methods of Kline and McClintock.[10] The uncertainty in the measured Nusselt number at the lower Reynolds numbers was estimated to be approximately ±7.2%, and the uncertainty in the measured jet Reynolds number was estimated to be approximately ±1.7%, each at a confidence interval of 95%. Measurement of the higher Reynolds number cases was of a much lower uncertainty due to the increased current flowing through the heated foil, increased voltage drop accross the heated foil, as well as increased pressure level measured upstream of the venturi nozzle.

III. Results and Discussion

Results for the spatial distribution in Nusselt number obtained from the test rig with a double exit configuration are presented in Figure 4. The spatial dependence on Nusselt number is presented for both the x and y directions and the spatial dimensions have been non-dimensionalized based upon the impingement jet nozzle diameter. The intersection of each grid line represents the center of each impingement jet nozzle. Although these results were obtained via an IR camera with a fixed resolution of approximately 1.8 pixels/mm, the apparent smoothing of the results was due to the selection of 120 levels when using MATLAB's "contourf" plotting function. As can be seen, Nusselt number is highly spatially dependent. The spatial variation in Nusselt number appears to be symmetric with respect to both the x=0 and y=0 axes. This can be expected based on the geometric symmetry in the flow passages. This symmetry is not seen in the results of Huang et al. due to the asymmetry in their inlet flow.[3] At the core of the impingement jets, the convective heat transfer coefficient is the highest. At the center of the impingement jet array (x/D=0) cross flow is at a minimum, if at all, and the variation in Nusselt number is primarily a radial phenomenon.

As was mentioned, the measurement domain had to be reduced to observe only 45 jets for the double exit configuration due to challenges with the measurement technique near the connection of the stainless steel foil to the copper busbar. This reduction consisted of 1 row being truncated on the left and the right sides of the measurement domain. In the single exit configuration, the bending of the jet core was different from that of the double exit configuration, which resulted in an additional one half of a jet being truncated on each side of the measurement domain in order to include an integer number of rows of impingement jets, so that only 40 jets were included in the measurement domain. In the single exit configuration, this reduction consisted of 1 row being truncated on the left side of the measurement domain and 2 rows were truncated on the right side of the measurement domain.

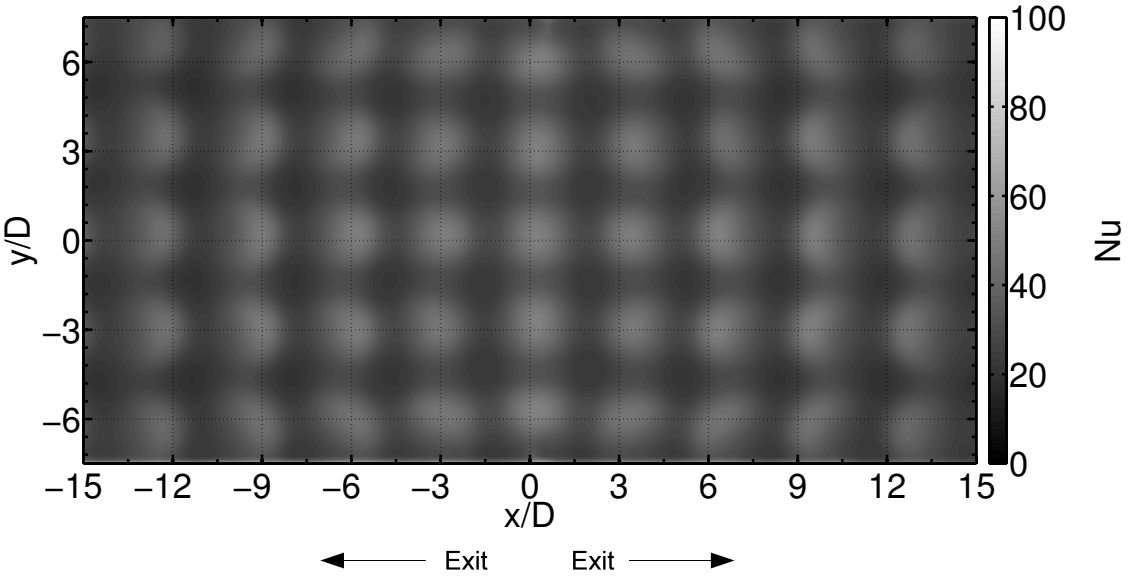

(a) Re=4,000

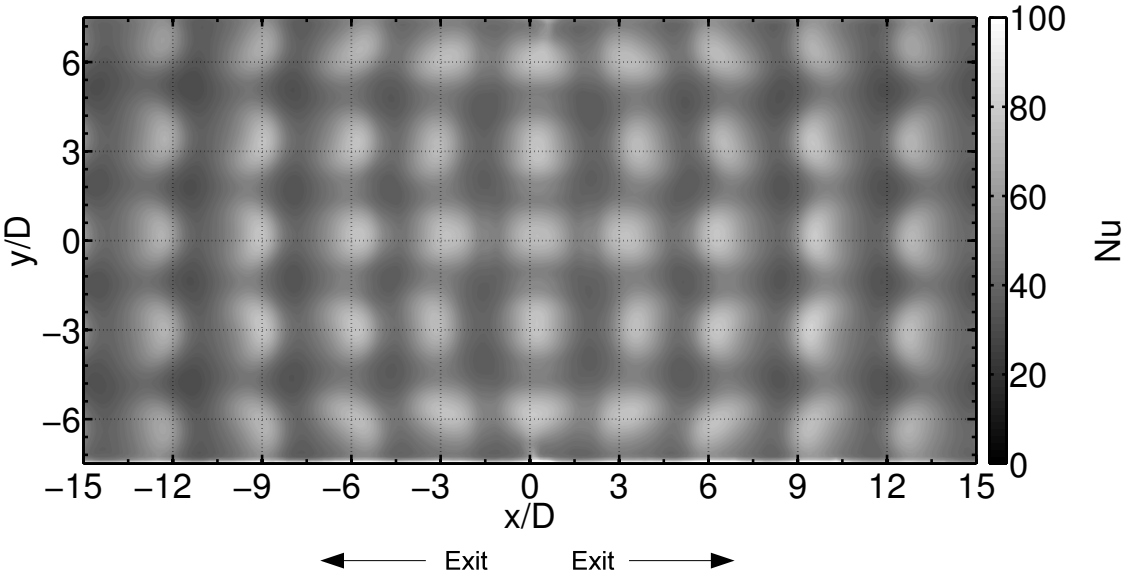

(b) Re=8,000

Figure 4. Double Exit - Time Averaged Nusselt Number

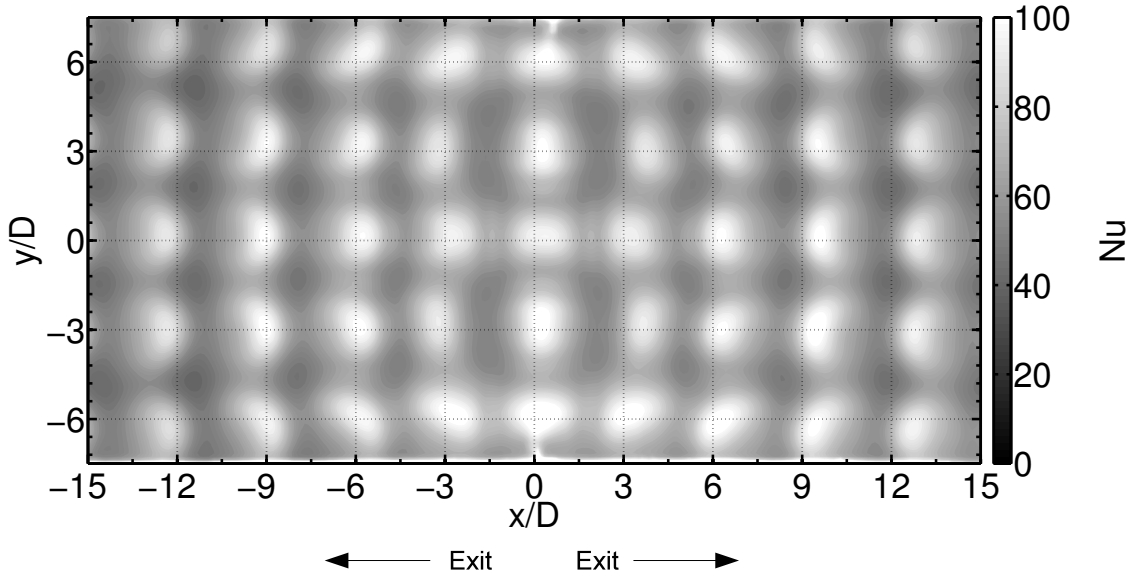

(c) Re=12,000

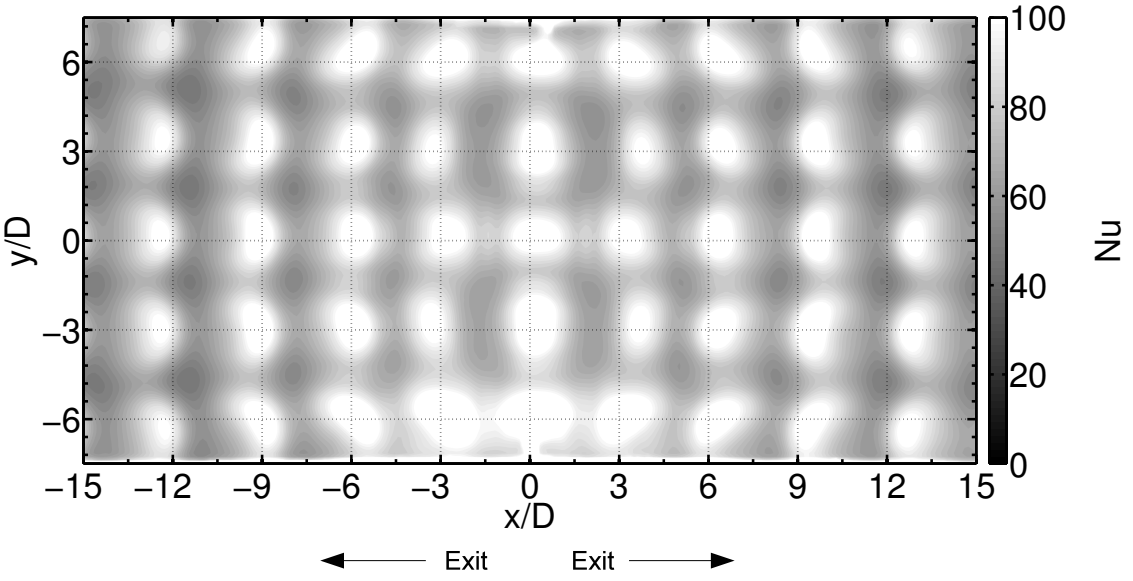

(d) Re=15,000

Figure 4. Double Exit - Time Averaged Nusselt Number

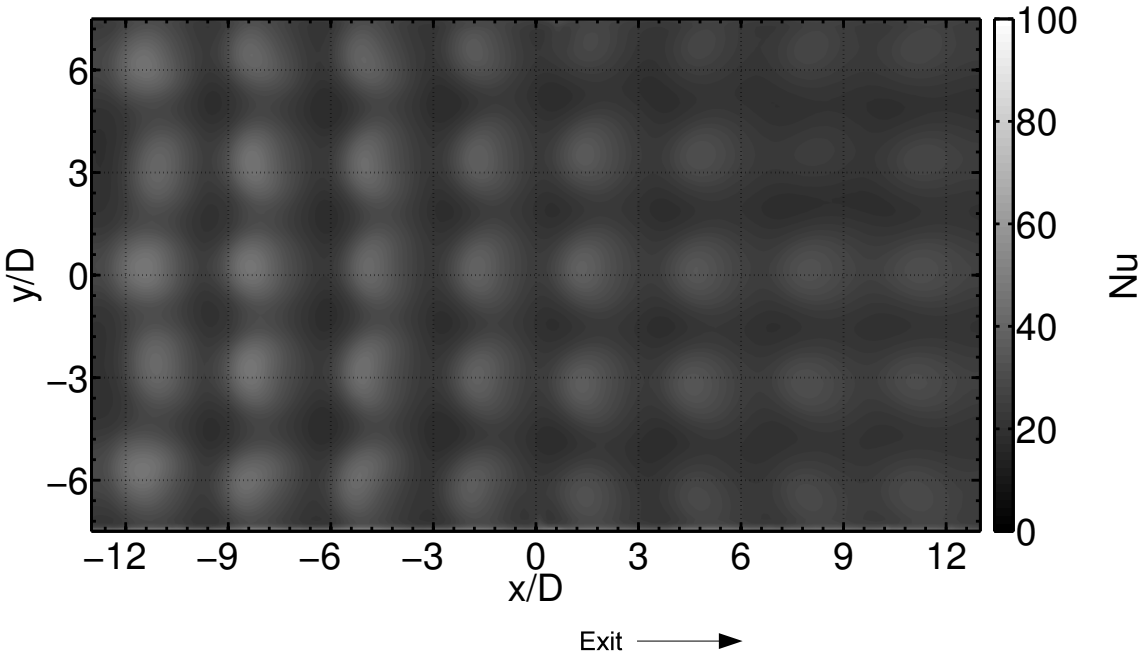

(a) Re=4,000

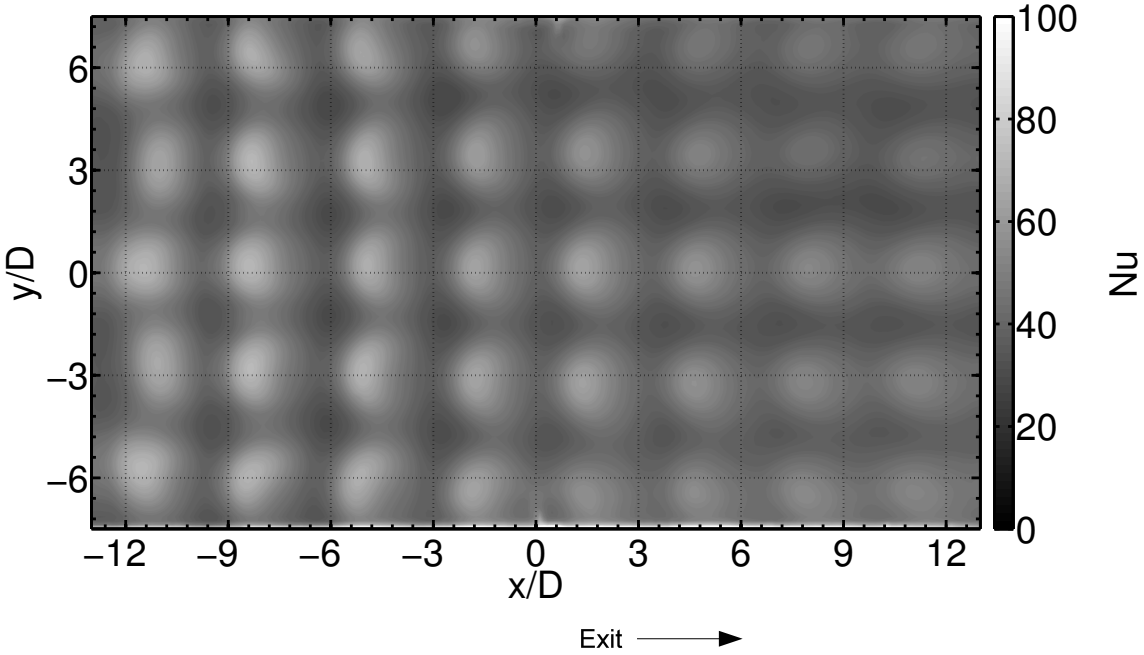

(b) Re=8,000

Figure 5. Single Exit - Time Averaged Nusselt Number

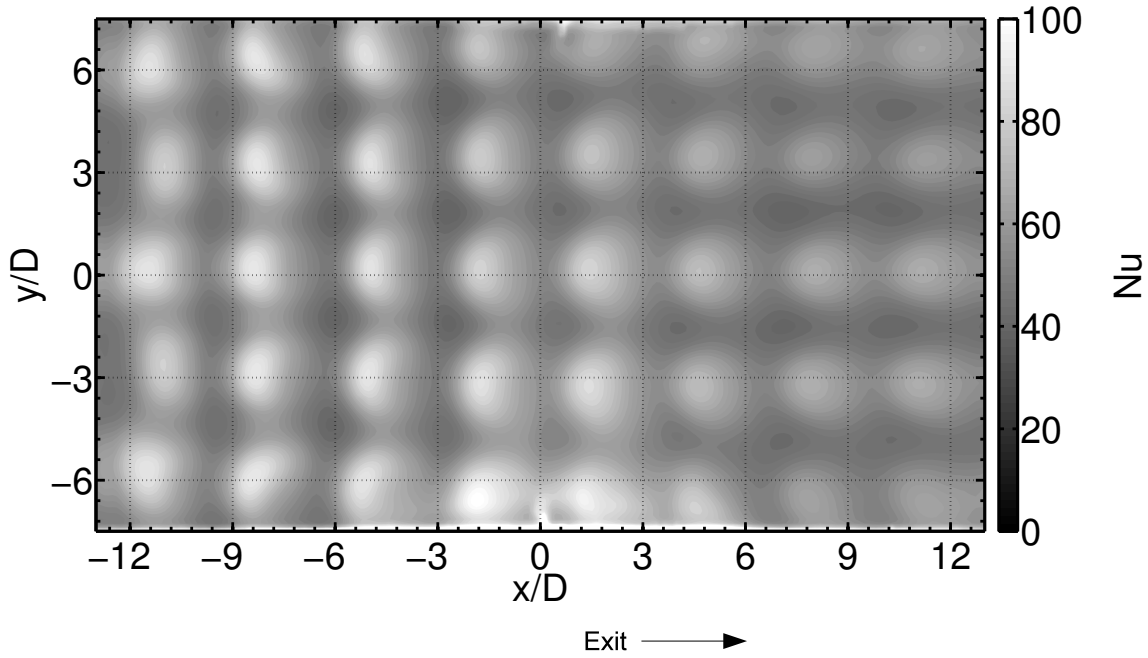

(c) Re=12,000

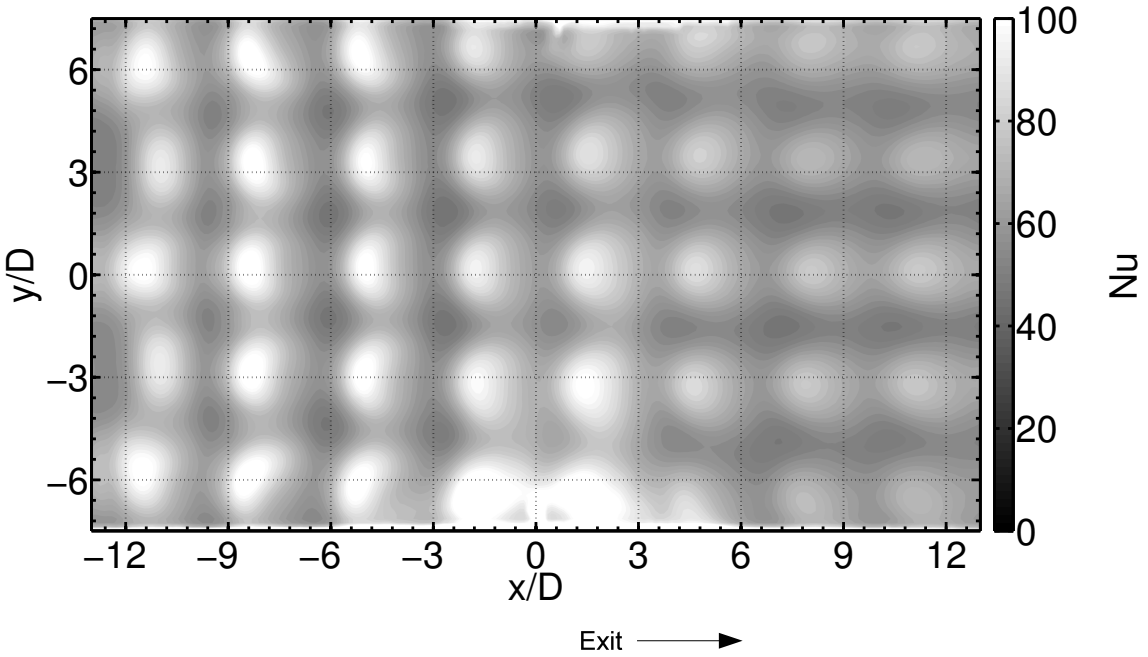

(d) Re=15,000

Figure 5. Single Exit - Time Averaged Nusselt Number

As the flow travels towards the exits, cross flow levels increase and the Nusselt number is no longer primarily a radial phenomenon. The cores of the jets are bent, and the region of highest heat transfer coefficient is no longer in line with the centers of the impingement jet nozzles. An interesting characteristic is that the region of highest heat transfer coefficient is shifted in both the x and y directions as the flow travels towards the exits. This phenomenon is also observed in the x direction in the results of Huang et al.[3] The shape of the region of highest heat transfer coefficient also changes with both spatial directions. These

variations in the y direction are believed to be caused by the additional space between the outer rows and the sidewalls when compared to the spacing between jets, rather than an interaction with the walls themselves.

It is evident that the heat transfer coefficient at the center of the jets is lower for the downstream jets (closer to the exhausts) compared to the upstream jets (near x=0). Additionally, the local heat transfer coefficient appears to decrease less rapidly with the distance from the jet centers for the downstream jets compared to the upstream jets. Because the cross flow levels are much higher closer towards the exits, the cross flow is believed to facilitate enhanced mixing in the areas outside of the jet core, leading to the higher heat transfer coefficients outside of the jet core.

As can be seen when reviewing Figure 4, the Nusselt number is highly dependent upon jet Reynolds number. The Nusselt number has an obvious increase with an increase in Reynolds number, as can be expected. In an effort to provide consistency in comparing results from multiple cases, a fixed scale of 0 to 100 has been selected for all contours of Nusselt number. The higher Reynolds number cases have some saturation in the contours presented. As a result, it is advised that the results for spanwise average Nusselt number be compared in order to gain more quantitative insight of Nusselt Number.

Figures 5 present results for time averaged Nusselt number for the single exit configuration for each jet Reynolds number. As can be seen, heat transfer coefficient is highest at the left which corresponds to the closed end where cross flow is at a minimum. Heat transfer coefficient is lowest at the right, which corresponds to the location closest to the exit, because cross flow is at maximum near the exit. Similarly to Figure 4, as cross flow is increased, heat transfer coefficient appears to reduce less rapidly with the distance from the center of the jet core. In Figures 5, this effect is more pronounced closer towards the exit due to the increased level of cross flow for all Reynolds numbers.

When comparing Figure 5 for the single exit configuration to Figure 4 for the double exit configuration it is interesting to note that, in addition to the reduction in heat transfer coefficient as the flow progresses towards the single exit, there is also a staggering of the regions of highest heat transfer coefficient near the left side (closed end) of the measurement domain. Near x/D≈-12 and y/D≈ ±3 the regions of highest heat transfer coefficient are shifted in the opposite x direction as the regions of highest heat transfer coefficient near x/D≈-12 and y/D≈6, 0, and -6. Although not presented in this document, animations of unsteady Nusselt number were generated using the 34.26 seconds of data and reviewed, and did not indicate that the staggering effect was an unsteady phenomenon.

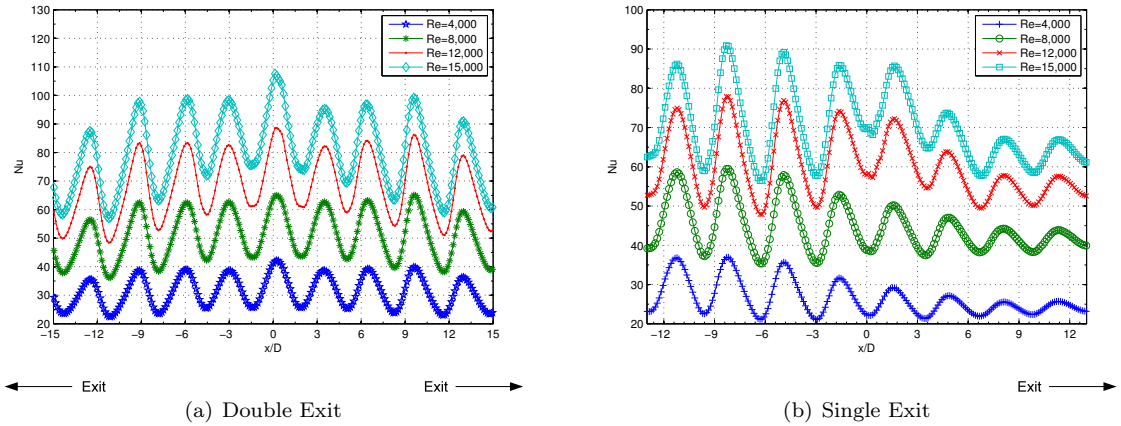

(a) Double Exit (b) Single Exit

Figure 6. Time and Spanwise Averaged Nusselt Number

Figure 6(a) presents a time and spanwise averaged Nusselt number for all Reynolds numbers with two exits. The vertical grid lines represent the location of the impingement jet nozzles. As can be seen, the time and spanwise averaged Nusselt number has a decreasing trend with distance from the center of the impingement jet array. Figure 6(b) presents the time and spanwise average Nusselt number for all Reynolds numbers and a single exit configuration. As with the double exit cases, with an increasing amount of cross flow, the maximum time and spanwise averaged Nusselt number is decreased and the minimum time and spanwise averaged Nusselt number is increased. It is interesting to note that for the single exit configuration the jet near x/D=-9 has a higher peak than the upstream jet near x/D=-12 which experiences reduced cross flow. As was mentioned in Section II, when the air reaches the pressure chamber it is believed to be at a

nearly uniform velocity and static pressure throughout due to the series of meshes shown in Figure 2 which serve to condition the flow. Because of the flow conditioning present in the test rig, this unanticipated feature is not believed to be due to an incorrect flow or pressure distribution in the plenum. Without conducting detailed three dimensional flow visualization, insufficient data has been collected to provide a thorough explanation. Similar results were also seen in the research of Huang et al.[3] for both of their single exit cases (flow orientation 1 and flow orientation 3). In their study, the effect was especially pronounced for flow orientation 3. Another interesting feature of the single exit configuration is that with the increased cross flow levels, there seems to be somewhat of a critical cross flow level at a position of x/D=3 where the time and spanwise averaged Nusselt number tends to decrease more rapidly for the higher jet Reynolds number cases, particularly at a jet Reynolds number of 15,000.

Figures 7(a) to 7(d) compare time and spanwise average Nusselt for the single and double exit configurations, at the same Reynolds number. It is evident that the time and spanwise averaged Nusselt number is significantly higher for the majority of the surface for the double exit configuration (including the peaks and troughs) for all Reynolds numbers studied. There is an extreme difference for all cases towards the right half of the measurement domain due to high cross flow effects.

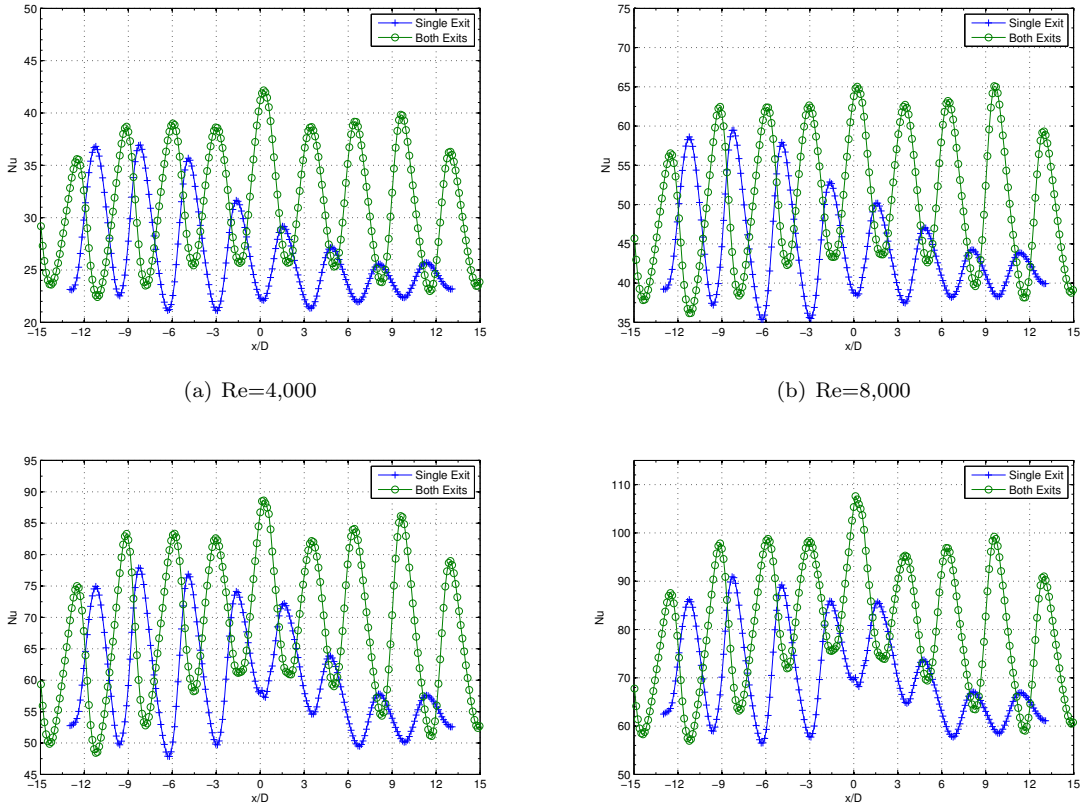

(a) Re=4,000

(b) Re=8,000

(c) Re=12,000

(d) Re=15,000

Figure 7. Double Exit vs Single Exit - Time and Spanwise Averaged Nusselt Number

Due to the unique nature of the geometry presently studied, no similar study has been identified in the public domain which could be used for comparison of the spatial results presented in Figures 4 to 7. The spatial variation in Nusselt number seen in the present work shows qualitative similarities to studies presented by Huang et al., and Gao, among others, which studied the spatial variation in target surface Nusselt number.[3,11]

Figure 8 shows the time and overall surface area averaged Nusselt number (Nu_{mean}) for all cases studied in the present work, as well as area averaged results from Huang et al.,[3] and a correlation by Florschuetz et al.[12] All results are nearly linear with respect to jet Reynolds number. Each group of researchers also showed that, relative to their own results, the area averaged Nusselt number is also dependent upon cross flow levels, although more weakly than the jet Reynolds number within the ranges studied. The work of Huang et al.,

used the same target spacing as the present work, but featured a different inlet flow configuration and utilized a rectangular hole pattern of x/D=y/D=4. Because of the asymmetry in their inlet flow configuration, two different single exit configurations were studied. The first had the inlet and exhaust in a co-flow arrangement, and the second had the inlet and the exhaust in a counterflow arrangement. Huang's team also utilized a transient liquid crystal thermography technique which featured a different thermal boundary condition on the target surface. These differences in flow geometry, experimental technique, as well as target surface thermal boundary condition may explain the differences in the area averaged Nusselt number shown in Figure 8.

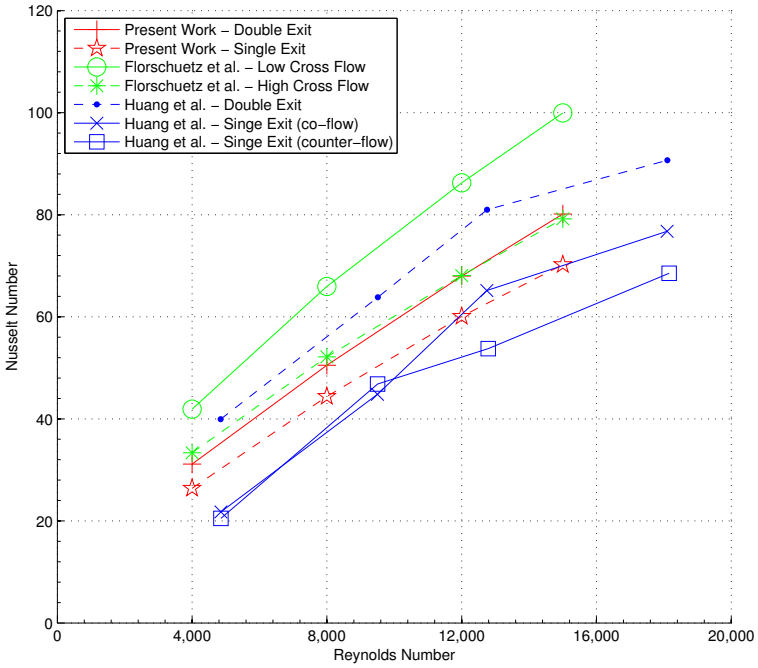

Figure 8. Area Averaged Nusselt Number

Area averaged Nusselt number determined using correlations provided by Florschuetz et al. also differed from that of the present work. Their correlation accounted for cross flow intensity, target spacing, hole pitch, Reynolds number, as well as Prandtl number. It is important to note that the correlation of Florschuetz et al. was developed using experimental data which featured minimum hole pitches of x/D=5 and y/D=4. As a result, the use of their correlation for the hole pitch of x/D=y/D=3 for the present study is considered an extrapolation. The results presented in Figure 8 using Florschuetz et al.'s correlation have attempted to mimic the single and double exit configurations of the present work by accounting for appropriate levels of cross flow. The high cross flow case corresponds to a single exit configuration and the low cross flow case corresponds to a double exit configuration. The experimental technique of Florschuetz et al. featured a target surface consisting of segmented copper bar heaters in which the power was individually controlled.[2] Due to the high thermal conductivity of copper, the temperature within each bar was essentially uniform, and the temperature of each bar was monitored with a thermocouple. The input power to each bar was adjusted until a nearly uniform temperature was achieved across the target surface. The deviations in the present results from the area averaged Nusselt number obtained using the correlation of Florschuetz et al. is believed to be due to the use of their correlation outside of their tested hole pitch and the differences in experimental techniques used.

IV. Conclusions

Experiments were performed to study the heat transfer characteristics of an array of 55 impingement jets with a constant heat flux boundary condition. Through the use of a steady state infrared thermography technique, accurate time averaging of unsteady convective heat transfer characteristics was conducted. Results for target surface Nusselt number have been presented for jet Reynolds numbers of 4,000, 8,000, 12,000, and 15,000 for a fixed target spacing of three jet diameters (z/D=3). Two cross flow configurations have been studied through the use of both a single exit, and a double exit configuration. The results show a strong dependency between the Nusselt number and the impingement jet Reynolds number. The time averaged Nusselt number increases with increasing jet Reynolds number in both the local and spanwise averaged values. The Nusselt number is also impacted by the exit flow configuration, although more weakly than jet Reynolds number for the range studied in the present work. The larger cross flow accumulation of the single exit configuration reduces the time averaged Nusselt number in both the local and spanwise averaged values, regardless of Reynolds number studied. In all cases studied, highly localized heat transfer characteristics were observed.

The spatial variation in target surface Nusselt number of the present results show qualitatively agreement with results presented by previous researchers. The area averaged target surface Nusselt number has been compared to data provided by Huang et al. and a correlation by Florschuetz et al.. No other study has been identified which features more similar flow geometry to that of the present work. The results from all researchers considered show similar trends with increases in Reynolds number as well as cross flow. Quantitative differences between results from each group of researchers may be explained by geometric as well as experimental differences between each of the studies.

Acknowledgments

This research project was supported by both the Dayton Area Graduate Studies Institute Student Fellowship Program and the Air Force Research Laboratory Summer Research Program. Their support is greatly appreciated.

References

[1]Kercher, D. and Tabakoff, W., ''Heat Transfer by a Square Array of Round Air Jets Impinging Perpendicular to a Flat Surface Including the Effect of Spent Air,'' *J. Eng. Power*, Vol. 92, No. 1, 1970, pp. 73--82.

[2]Florschuetz, L., Metzger, D., Takeuchi, D., and Berry, R., ''Multiple Jet Impingement Heat Transfer Characteristic: Experimental Investigation of In-Line and Staggered Arrays with Crossflow,'' NASA Contractor Report 3217, Department of Mechanical Engineering, Arizona State University, Tempe, January 1980.

[3]Huang, Y., Ekkad, S., and Han, J., ''Detailed Heat Transfer Distributions Under an Array of Orthogonal Impinging Jets,'' *Journal of Thermophysics and Heat Transfer*, Vol. 12, No. 1, 1998, pp. 73--79.

[4]Kanokjaruvijit, K. and Martinez-botas, R., ''Jet Impingement on a Dimpled Surface with Different Crossflow Schemes,'' *International Journal of Heat and Mass Transfer*, Vol. 48, No. 1, 2005, pp. 161--170.

[5]Wang, T., Lin, M., and Bunker, R., ''Flow and Heat Transfer of Confined Impingement Jets Cooling Using a 3-D Transient Liquid Crystal Scheme,'' *International Journal of Heat and Mass Transfer*, Vol. 48, No. 23-24, 2005, pp. 4887--4903.

[6]Esposito, E., Ekkad, S., Kim, Y., and Dutta, P., ''Novel Jet Impingement Cooling Geometry for Combustor Liner Backside Cooling,'' *Journal of Thermal Science and Engineering Applications*, Vol. 1, No. 2, 2009, pp. 021001--8.

[7]Ou, S. and Rivir, R., ''Shaped-Hole Film Cooling With Pulsed Secondary Flow,'' *ASME Paper*, No. GT2006-90272, International Gas Turbine Institute, 2006.

[8]Bejan, A., *Convection Heat Transfer*, Wiley, 2004, p. 198.

[9]Schroder, A., *Experimental and Numerical Study of Impingement Jet Heat Transfer*, Master's thesis, University of Cincinnati, May 2011.

[10]Kline, S. and McClintock, F., ''Describing Uncertainties in Single-Sample Experiments,'' *Mechanical engineering*, Vol. 75, No. 1, 1953, pp. 3--8.

[11]Gao, L., *Effect of Jet Hole Arrays Arrangement on Impingement Heat Transfer*, Master's thesis, Louisiana State University, 2003.

[12]Florschuetz, L., Truman, C., and Metzger, D., ''Streamwise Flow and Heat Transfer Distributions for Jet Array Impingement with Crossflow,'' *Journal of Heat transfer*, Vol. 103, 1981, pp. 337--342.